

Hydrodynamics of Lorentz symmetric systems: a quantum Monte Carlo study

Adrien Reingruber,^{1,*} Kitinan Pongsangangan,^{2,3,†} Fakher Assaad,^{1,4,‡} and Maksim Ulybyshev^{1,§}

¹*Institut für Theoretische Physik und Astrophysik,
Universität Würzburg, 97074 Würzburg, Germany*

²*Department of Physics, Faculty of Science, Mahidol University, Bangkok 10400, Thailand*

³*Institute of Theoretical Physics, Technische Universität Dresden, 01062 Dresden, Germany*

⁴*Würzburg-Dresden Cluster of Excellence ct.qmat, Am Hubland, 97074 Würzburg, Germany*

We present a study on the hydrodynamic behavior of charge current in a Lorentz symmetric system: graphene at charge-neutrality. The momentum flow is completely decoupled from the charge current in this regime, since the electrons and holes propagate in opposite directions with exactly equal distribution functions. Instead of Navier-Stokes equations for the velocity field, we derive similar equations directly for the charge current. This eliminates the need for any coupling between the velocity field and charge current to explain the experimentally observed hydrodynamic flow profiles in graphene at half-filling. In this framework, the current diffusion coefficient replaces viscosity. To support this, we performed an extensive quantum Monte Carlo study, directly simulating samples with disordered edges using the underlying microscopic interacting quantum Hamiltonian. For the first time, we observe hydrodynamic behavior of the charge current in such simulations, extracting current profiles and a current diffusion coefficient whose temperature dependence qualitatively agrees with predictions from Boltzmann transport theory.

Keywords: Graphene, Transport Hydrodynamics, Quantum Monte Carlo, Boltzmann theory

Introduction.

Strongly correlated systems provide an exciting playground to study the electronic transport due to the presence of multiple scattering mechanisms generating different time scales. In particular, when the particle-particle relaxation time, τ_{pp} , is much shorter than the diffusive scattering time, τ_{diff} (arising from factors such as defects), the system transitions from Ohmic electron transport to a regime resembling the hydrodynamics of a viscous fluid [1–6]. This transition significantly alters the current flow profiles, depending on the sample geometry. For narrow conductors, a simple parabolic Poiseuille profile can be expected, while more complex structures such as vorticity may emerge in other cases [7]. The dominance of particle-particle scattering parallels the behavior of strongly correlated quantum field theories (QFTs) [8, 9], and it has been proposed that in graphene at the charge neutrality point (CNP), we may approach the lower bound for the ratio of shear viscosity to entropy density [4], a limit initially derived for a broad class of strongly correlated QFTs [9].

Recent advances in experimental techniques have provided an additional boost to these studies. Within now exceptionally clean graphene samples encapsulated between two layers of boron nitride, particle-particle collisions become the dominant scattering mechanism, thereby shifting electronic transport to the hydrodynamic regime. Combined with new imaging techniques, this development enables direct visualization of hydro-

dynamic flow profiles and measurement of viscosity in graphene [10–13].

However, an important subtlety arises in detecting hydrodynamic flow at CNP. Viscosity appears in the Navier-Stokes (NS) equations governing the velocity field \vec{u} , and it essentially describes the dynamics of momentum density under external forces. Imaging techniques like those in [12, 13] visualize the stray magnetic field, capturing the charge current flow rather than the momentum distribution. Away from half-filling, this is not problematic, as the imbalance between electrons and holes enables a direct link between momentum flow and charge current. At CNP, however, momentum flow is entirely decoupled from the electric current since the electrons and holes propagate in opposite directions with equal average momenta. Consequently, the momentum density governed by the NS equations remains unaffected by an external electric field [7], staying uniform and averaging to zero. This implies that a Poiseuille flow profile cannot be expected for the charge current. Instead, a temperature gradient must be applied to drive momentum density flow [14, 15].

Contrary to these expectations, current density measurements at CNP [12] reveal a current flow closely following the Poiseuille profile, though the charge density should be assumed to correspond to chemical potential $\mu = k_B T$ even at CNP. Under this assumption, the kinematic viscosity ν obtained by fitting experimental data with NS equation solutions aligns well with theoretical predictions for shear viscosity [4]. This finding suggests the presence of a mechanism that couples charge current with the hydrodynamic velocity field, even at CNP.

Our paper addresses this specific issue. We develop a theoretical description, excluding any mechanism that couples the velocity field and charge current at CNP. Instead, we derive equations for the charge current density

* adrien.reingruber@uni-wuerzburg.de

† kitinan.pon@mahidol.ac.th

‡ fakher.assaad@uni-wuerzburg.de

§ maksim.ulybyshev@uni-wuerzburg.de

from the underlying Boltzmann equation. In this framework, a different transport coefficient, the current diffusion coefficient ζ , replaces viscosity, allowing us to write the same NS-type equations directly for the charge current density without any reference to the velocity field.

In order to support this statement, we conduct an extensive quantum Monte Carlo (QMC) study of charge current flow in graphene, allowing us to obtain hydrodynamic charge current profiles in a well-controlled environment. The dominant scattering mechanism is particle-particle collisions, since the bulk volume of the simulated samples is defect-free, and phonons are absent in our microscopic Hamiltonian. On the other hand, QMC provides exact results for a given microscopic quantum Hamiltonian when the sign problem is absent [16–20], which is indeed the case at CNP. Our results are directly applicable to freestanding graphene with unscreened Coulomb interaction, as we utilize an interacting quantum Hamiltonian verified by comparing QMC calculations with the experimental data for the renormalized Fermi velocity v_F [21]. We also pay special attention to the microscopic mechanisms governing boundary conditions, which are essential for creating inhomogeneities in current flow thus playing a crucial role in demonstrating hydrodynamic behavior of charge current at CNP.

Kinetic theory approach.

The electronic transport in hydrodynamic regime is dominated by momentum conserving electron-electron collisions¹ with characteristic time scale τ_{ee} [22–25]. It means that diffusive mechanisms have significantly larger timescales and we have well defined quasi-particles following the Fermi distribution function $f(\vec{k}, \vec{r}, t)$ depending on space, momentum and time. It obeys the Boltzmann equation [26]:

$$\left(\frac{\partial}{\partial t} + \vec{v}_\lambda \cdot \nabla_{\vec{r}} + \vec{E} \cdot \nabla_{\vec{k}} \right) f_\lambda(\vec{k}, \vec{r}, t) = \mathcal{I}_{ee}^{\text{col}} \quad (1)$$

We consider a two-component model with electrons and holes ($\lambda = \pm$), as the degrees of freedom in graphene at CNP and at a non-zero temperature. The electron-electron and electron-hole long-range Coulomb interactions provide a scattering channel sufficient to obtain a finite electrical conductivity. We adopt a minimal model admitting the minimal conductivity into the Eq. (1) [15]:

$$\partial_t f_\pm + \vec{v}_\pm \cdot \vec{\nabla}_{\vec{k}} f_\pm - e\vec{E} \cdot \vec{\nabla}_{\vec{k}} f_\pm = \mp \frac{\delta f_+ - \delta f_-}{\tau_{ee}}. \quad (2)$$

Here f_\pm defines the distribution function for electrons in the conduction (+) and valence (−) bands with the corresponding energy $\epsilon_\pm = \pm v_F k$ and velocity $\vec{v}_\pm = \vec{\nabla}_{\vec{k}} \epsilon_\pm = \pm v_F \vec{k}/k$ (we consider only Dirac dispersion relation). In thermal equilibrium $f_\pm = (e^{\pm v_F k/T} + 1)^{-1}$ at CNP. The

mean free time τ_{ee} is treated in the relaxation time approximation.

The equation for charge current is obtained from the Boltzmann equation (2) by multiplying both sides by $N e \vec{v}_\pm$ with $N = 4$ accounting for valley and spin degeneracy and integrating over momentum:

$$\partial_t \vec{j}^n + \partial_m \mathcal{J}^{nm} + e E^m \mathcal{E}^{mn} = -\frac{j^n}{\tau_{ee}/2}. \quad (3)$$

Here $\vec{j} = \vec{j}_+ + \vec{j}_-$ is the total charge current density and the current densities of electrons (\vec{j}_+) and holes (\vec{j}_-) are defined as $\vec{j}_\pm = N e \int d\vec{k} \vec{v}_\pm \tilde{f}_\pm$. The redefined distributions are: $\tilde{f}_+ = f_+$ for the conduction band and $\tilde{f}_- = f_- - 1$ for the valence band. The current flux tensor $\mathcal{J}^{nm} = \mathcal{J}_+^{nm} + \mathcal{J}_-^{nm}$ plays a role comparable to the stress-energy tensor in the NS equation. The tensor $\mathcal{E}^{mn} = \mathcal{E}_+^{mn} + \mathcal{E}_-^{mn}$ is coupled to the external electric field, remaining non-zero even at CNP. These tensors are defined via a shorthand notation as $\mathcal{J}^{nm}_\pm = N e \int d\vec{k} v_\pm^n v_\pm^m \tilde{f}_\pm$ and $\mathcal{E}^{mn}_\pm = N e \int d\vec{k} \partial_m v_\pm^n \tilde{f}_\pm$. \mathcal{E}^{mn} is diagonal for Dirac fermions: $\mathcal{E}^{mn} = -(2T e \ln 2)/\pi \delta^{mn} \equiv -e\mathcal{E} \delta^{mn}$.

The homogeneous and stationary solution of the current equation (3) gives the critical conductivity $\sigma_Q = e\mathcal{E}\tau_{ee}/2 = e^2(T \ln 2)\tau_{ee}/\pi$ [15]. In the presence of a current gradient $\nabla_x j_y(x)$, the current diffusion coefficient represents a material's ability to conduct a current flux flowing in x -direction to transfer and, as a result, equilibrate the y -current in between layers of the fluid (see Fig. 1):

$$\mathcal{J}^{nm} = -\zeta \partial_n j^m. \quad (4)$$

This is to be compared with kinematic viscosity which represents conductivity of momentum flux in the presence of a momentum density gradient [22]. At CNP in graphene, the momentum density is completely decoupled from the electric current due to the emergent Lorentz symmetry. The current diffusion coefficient is, thus, distinguished from the kinematic viscosity.

The final stationary ($\partial_t \vec{j} = 0$) current equation is

$$-\zeta \nabla^2 j^n + e E^m \mathcal{E}^{mn} = -\frac{j^n}{\tau_{ee}/2}, \quad (5)$$

augmented by the continuity equation $\vec{\nabla} \cdot \vec{j} = 0$. Note the similarity with the NS equation for velocity. If we solve it for the stripe of width w , oriented along the y -axis (same direction as electric field), we get the catenary curve

$$j_y(x) = \left(\sigma_Q + \sigma_B \frac{\cosh(Ax)}{\cosh(A\frac{w}{2})} \right) E_y, \quad (6)$$

where $A = \sqrt{(e\mathcal{E})/(\zeta\sigma_Q)}$, and σ_B is defined by the boundary conditions.

In order to estimate ζ , we go back to the stationary, but inhomogeneous, Boltzmann equation

$$\vec{v}_\lambda \cdot \nabla_{\vec{r}} f_\lambda(\vec{k}, \vec{r}, t) = \mathcal{I}_{ee}^{\text{col}}. \quad (7)$$

¹ Umklapp processes are neglected

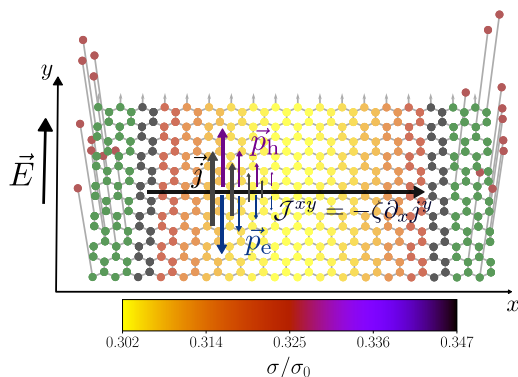


FIG. 1. Scheme of the smallest simulated sample consisting of 18 stripes of carbon atoms. We impose periodical boundary conditions in y-direction, and open boundary with disorder (adatoms, shown in red) in x-direction. We place 8 (2) adatoms randomly on the edge (next-to-the-edge) stripes. The electric field $\vec{E} = E\vec{e}_y$ drives electron and hole fluids in the opposite directions. While the momentum density remains trivially homogeneous, the current distribution has non-trivial gradient $\vec{\nabla}\vec{j} \neq 0$. As a result, there exists the current flux \mathcal{J}^{xy} diffusing from the region with high current density to the region with small current density. This results in the conductivity profile, visible through the heatmap corresponding to Fig. 2 (d). The green sites on the edges correspond to the stripes with disorder and are not taken into account when fitting the conductivity profiles. $\sigma_0 = 1/4$ in the units of e^2/h .

The collision integral $\mathcal{I}_{ee}^{\text{col}}$ for the long-range Coulomb interaction was derived in [26] from a Schwinger-Keldysh quantum field theory (see the Supplementary Material (SM) for details) up to the second order in the effective fine structure constant of graphene. The above Boltzmann equation was previously solved up to the leading-log approximation by the variational method [27], for the critical conductivity [26], shear viscosity [4], and spin conductivity [28] of graphene. Here we apply the same approach to compute the current diffusion coefficient ζ . To the leading-log approximation, the result is

$$\frac{\zeta}{a^2 t} = C(\epsilon a t)^2 \frac{t}{T}, \quad (8)$$

with dimensionless $C = 25.76$. t is the C-C hopping and a the unit lattice vector length in graphene. Eq. (8) is strictly speaking valid at low temperatures, $T/t \lesssim 0.3$, at which the dispersion relation is approximately linear, nevertheless we expect that the general $1/T$ dependence remains, even beyond the Dirac approximation.

Microscopic description and QMC simulations

In order to demonstrate hydrodynamics of charge current at the CNP in *ab initio* QMC simulations, we consider free standing graphene strips similar to the one shown in Fig. 1. Disordered edges in x-direction create a non-uniform current flow across the strip.

We simulate the following quantum Hamiltonian with

long-range Coulomb interactions (LRC)

$$\hat{H}_{\text{LRC}} = - \sum_{\langle i,j \rangle, \sigma} t(\hat{a}_{i,\sigma}^\dagger \hat{a}_{j,\sigma} + \text{h.c.}) + \frac{1}{2} \sum_{ij} V_{ij} \hat{q}_i \hat{q}_j, \quad (9)$$

where $\langle i,j \rangle$ are nearest neighbor sites. $\hat{a}_{i,\sigma}$ are annihilation operators for electrons with spin $\sigma = \uparrow, \downarrow$ on site i and V_{ij} is a matrix of unscreened Coulomb interactions between the charge carriers described by the charge operator $\hat{q}_i = \sum_{\sigma} (\hat{a}_{i,\sigma}^\dagger \hat{a}_{i,\sigma} - \frac{1}{2})$ at site i . The hopping is $t = 2.7 \text{ eV}$ and the matrix of potentials is taken from [21], where it was used to reproduce the experiments on free standing graphene.

Since the lattice size is limited in QMC simulations, we can not consider broken edges like in [14]. Instead, disorder is introduced by random placing of adatoms on top of the sites along the two edges (see Fig. 1). The hopping between adatoms $\hat{c}_{i,\sigma}^\dagger$ and regular sites $\hat{a}_{i,\sigma}^\dagger$, is described by a hybridization Hamiltonian $\hat{H}_{\text{adatom}} = \sum_{i,\sigma} t'(\hat{a}_{i,\sigma}^\dagger \hat{c}_{i,\sigma} + \text{h.c.})$, with $t' = 10t$, roughly corresponding to hydrogen adatoms on top of carbons [29]. The full microscopic Hamiltonian of the system is therefore $\hat{H} = \hat{H}_{\text{adatom}} + \hat{H}_{\text{LRC}}$.

The Hamiltonian is simulated using the finite temperature auxiliary field Quantum Monte Carlo method [30–32] with continuous fields [18, 19], due to the LRC Coulomb interaction. Because of particle-hole symmetry, the system is sign-problem free, and the simulations are carried out with the Algorithm for Lattice Fermions (ALF) [33]. In order to compute the current profile, we measure the diagonal element of the local DC conductivity tensor $\sigma_{yy}(\omega)$. It is obtained using the stochastic analytical continuation method (SAC) [34–36] via Green-Kubo relations from the Euclidean current-current correlator [37–40]. In order to justify the stability of the SAC method, we reproduced the same results from the middle-point of the current-current correlator [41]. Details can be found in SM.

We start from the analysis of the boundary conditions imposed by the adatoms at the edge. Frequency profiles of the free conductivity obtained from the tight-binding part of the full Hamiltonian \hat{H} show that the imposed boundary conditions are substantially different for different frequencies (Fig. 2a and 2b). Small frequencies (Drude peak regime) have almost no-slip boundary conditions with the conductivity sharply decreasing at the edge, while optical frequencies around the Dirac plateau ($\omega \approx 0.5$) have reverse boundary conditions with a conductivity at the edge larger than in the bulk. If we switch to the interacting case (Fig. 2c), the Drude peak disappears from the $\sigma(\omega)$ profiles due to a large electron-electron scattering rate, and we are left with the Dirac plateau regime extending to small frequencies, a situation already observed in [40, 42]. Thus we have boundary conditions similar to the larger frequency regime of the free case with the current falling towards the bulk except for the stripe located exactly at the edge. Hence we fit our

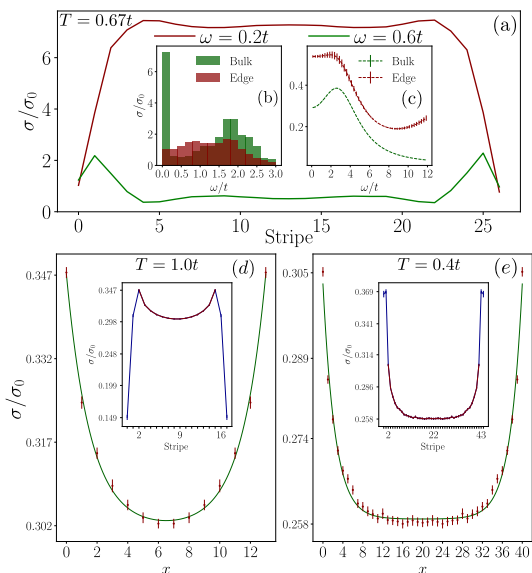


FIG. 2. (a) Local conductivity profiles at two different frequencies for the free tight-binding model with randomly distributed adatoms at the edges. (b) $\sigma(\omega)$ profiles for the same free Hamiltonian in the middle of the sample ("bulk") and at the edge. Since the conductivity is a series of delta-functions in the free case, each bar in the plot shows the sum of weights of these delta functions in the corresponding interval of frequencies. (d,e) Local DC conductivity profiles across the sample in the interacting case for two different temperatures. SAC data, obtained from the Euclidean current-current correlator. Only points used for the fit are shown in the main plot, while the full profiles are displayed in the insets: fit with catenary curve (green) starts from the point next to the maximum in the full conductivity profile. (c) $\sigma(\omega)$ for the interacting case. "Bulk" profile corresponds to the middle of the sample. "Edge" profile corresponds to the peak in the local DC conductivity profile across the sample (see the inset in figure (d)).

QMC profiles in the bulk using the catenary curve (6) with $\sigma_B > 0$.

The conductivity profiles computed for the full interacting Hamiltonian are displayed in Fig. 2d and 2e, with more profiles shown in SM. In order to have a high density of temperature excitations for our small lattice sizes (in another words, to satisfy the condition $\omega \ll T$ for hydrodynamic regime [26]), the simulations were carried out for high temperatures, and the width of the sample is increased inversely proportional to the lowering T . The data reproduces remarkably well the expected conductivity profiles of Eq. 6. From them, we extract the values of ζ , also computing the diagonal elements of the tensor \mathcal{E} using the exact interacting Green Functions obtained in QMC (see SM for the details). The resulting temperature dependent ζ is presented in Fig. 3. Fitting at $\epsilon = 1$ (free-standing graphene) yields the same power law function as in (8): $\zeta \sim 1/T^{1.09 \pm 0.14}$, but with $C = 5.67 \pm 0.46$. The difference between the theoretical expectation and QMC results can be attributed to the approximations used to

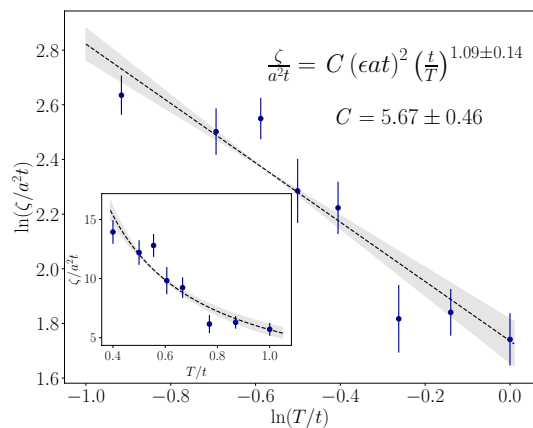


FIG. 3. Temperature dependent current diffusion coefficient ζ in log-log representation (main plot) and with linear scales (inset). Fit is shown with the dotted line and the error margin of the fitting function is shown in grey.

compute C in kinetic theory: 1) Dirac dispersion relation instead of the full expression for the honeycomb lattice; 2) Only tree-level diagrams in the collision integral in (7). The latter deficiency can be also connected to the importance of higher-order diagrams in the comparison of v_F renormalization with the perturbative RPA result reported in [21]. It seems that higher-order corrections to the scattering amplitudes play an important role in the transport properties of free-standing graphene.

Conclusion.

We showed that the hydrodynamic behavior of charge current in graphene at CNP can be explained without any coupling to the velocity field. Instead, an equation similar to the NS equations was derived for the charge current from a two-liquid (electrons and holes) Boltzmann formalism. In this case the current diffusion coefficient ζ substitutes the viscosity. This description is supported by unbiased *ab initio* QMC simulations, where we clearly observe the hydrodynamic current profiles. These profiles and $\zeta(T)$, extracted from them, agree qualitatively well with the aforementioned Boltzmann transport theory. As a consequence, the correct interpretation of the observed hydrodynamic profiles of charge current in graphene at CNP should be made in terms of the current diffusion coefficient, and not in terms of viscosity. Beyond the Lorentz-symmetrical case, these results can be extended to any system with particle-hole symmetry at half-filling. We expect the same picture for AB-stacked bilayer graphene with quadratic band touching or any narrow-gapped semiconductor with symmetric bands.

ACKNOWLEDGMENTS

KP thanks former collaborations and discussions with L. Fritz, H.T.C. Stoof, T. Ludwig, S. Grubinskas, P. Cosme, E. Di Salvo, T. Meng. MU thanks J. Schmalian

for discussions about the boundary conditions and AR thanks R. Meyer for insightful exchanges about hydrodynamics in QFT.

MU (AR) thanks the DFG for financial support under the projects UL444/2-1, Project number 495044360 (AS120/19-1, Project number 530989922). FFA acknowledges financial support from the DFG through the Würzburg-Dresden Cluster of Excellence on Complexity and Topology in Quantum Matter - *ct.qmat* (EXC 2147, Project No. 390858490) as well as the SFB 1170 on Topological and Correlated Electronics at Surfaces and Interfaces (Project No. 258499086). KP acknowledges funding by the Deutsche Forschungsgemeinschaft (DFG) via the Emmy Noether Programme (Quantum Design grant, ME4844/1, project- id 327807255), project A04 of the Collaborative Research Center SFB 1143 (project-id 247310070), and the Cluster of Excellence on Complexity and Topology in Quantum Matter *ct.qmat* (EXC

2147, project-id 390858490). We gratefully acknowledge the Gauss Centre for Supercomputing e.V. (www.gauss-centre.eu) for funding this project by providing computing time for the computation of the current-current correlator on the GCS Supercomputer SUPERMUC-NG at the Leibniz Supercomputing Centre (www.lrz.de, project number pn73xu), as well as the scientific support and HPC resources provided by the Erlangen National High Performance Computing Center (NHR@FAU) of the Friedrich-Alexander-Universität Erlangen-Nürnberg (FAU) under the NHR project b133ae to carry out the SAC analysis. NHR funding is provided by federal and Bavarian state authorities. NHR@FAU hardware is partially funded by the German Research Foundation (DFG) – 440719683. JUWELS [43] supercomputer was used for the calculation of \mathcal{E} tensor. The numerical calculations were carried out with the Algorithms for Lattice Fermions (ALF) library [33].

SUPPLEMENTARY MATERIAL

I. KINETIC THEORY APPROACH AND THE CALCULATION OF THE CURRENT DIFFUSION COEFFICIENT

In this section, we sketch the calculation of the current diffusion coefficient ζ from the kinetic theory approach reported in the main text.

A non-zero current density gradient, $\vec{\nabla} \vec{j} \neq 0$ drives a system out of equilibrium. A stationary, but inhomogeneous, state of the system obeys a Boltzmann equation reading as

$$\vec{v}_\lambda \cdot \nabla_{\vec{r}} f_\lambda(\vec{k}, \vec{r}, t) = \mathcal{I}_{ee}^{\text{col}}. \quad (10)$$

Here f_\pm defines the distribution function for Dirac electrons in the conduction (+) and valence (−) bands with the corresponding energy $\epsilon_\pm = \pm v_F k$ and velocity $\vec{v}_\pm = \vec{\nabla}_{\vec{k}} \epsilon_\pm = \pm v_F \vec{k}/k$ close to the K point in the Brillouin zone. The collision integral $\mathcal{I}_{ee}^{\text{col}}$ was derived from a Schwinger-Keldysh quantum field theory and is written in terms of the Coulomb interaction up to α^2 [26]. Here $\alpha = e^2/6\pi\hbar\epsilon a t$ defines effective fine structure constant of graphene, where t is C-C hopping, a the graphene unit cell length and ϵ is the dielectric constant defining the screening of the Coulomb potential by a substrate. The corresponding collision integral describes $2 \rightarrow 2$ scattering and reads as

$$\begin{aligned} \mathcal{I}_{ee}^{\text{col}} = & -\frac{2\pi}{v_F} \int_{\vec{k}_1, \vec{q}} \delta(k - k_1 - |\vec{k} - \vec{q}| + |\vec{k}_1 + \vec{q}|) R_1(\vec{k}, \vec{k}_1, \vec{q}) \\ & \left\{ f_\lambda(\vec{k}) f_{-\lambda}(\vec{k}_1) [1 - f_\lambda(\vec{k} - \vec{q})] [1 - f_{-\lambda}(\vec{k}_1 + \vec{q})] - [1 - f_\lambda(\vec{k})] [1 - f_{-\lambda}(\vec{k}_1)] f_\lambda(\vec{k} - \vec{q}) f_{-\lambda}(\vec{k}_1 + \vec{q}) \right\} \\ & -\frac{2\pi}{v_F} \int_{\vec{k}_1, \vec{q}} \delta(k + k_1 - |\vec{k} - \vec{q}| - |\vec{k}_1 + \vec{q}|) R_2(\vec{k}, \vec{k}_1, \vec{q}) \\ & \left\{ f_\lambda(\vec{k}) f_\lambda(\vec{k}_1) [1 - f_\lambda(\vec{k} - \vec{q})] [1 - f_\lambda(\vec{k}_1 + \vec{q})] - [1 - f_\lambda(\vec{k})] [1 - f_\lambda(\vec{k}_1)] f_\lambda(\vec{k} - \vec{q}) f_\lambda(\vec{k}_1 + \vec{q}) \right\}, \end{aligned} \quad (11)$$

with

$$\begin{aligned}
R_1(\vec{k}, \vec{k}_1, \vec{q}) &= 4 \left(\left| T_{++--}(\vec{k}, \vec{k}_1, \vec{q}) - T_{++--}(\vec{k}, \vec{k}_1, \vec{k} - \vec{q} - \vec{k}_1) \right|^2 \right. \\
&\quad \left. + (N-1) \left[\left| T_{++--}(\vec{k}, \vec{k}_1, \vec{q}) \right|^2 + \left| T_{++--}(\vec{k}, \vec{k}_1, \vec{k} - \vec{q} - \vec{k}_1) \right|^2 \right] \right), \\
R_2(\vec{k}, \vec{k}_1, \vec{q}) &= 4 \left(\frac{1}{2} \left| T_{++++}(\vec{k}, \vec{k}_1, \vec{q}) - T_{++++}(\vec{k}, \vec{k}_1, \vec{k} - \vec{q} - \vec{k}_1) \right|^2 + (N-1) \left| T_{++++}(\vec{k}, \vec{k}_1, \vec{q}) \right|^2 \right).
\end{aligned} \tag{12}$$

Here we introduce the short-hand:

$$T_{\lambda_1 \lambda_2 \lambda_3 \lambda_4}(\vec{k}, \vec{k}_1, \vec{q}) = \frac{V(\vec{q})}{2} \left(\mathcal{M}_{\vec{k}, \vec{k} - \vec{q}}^{\lambda_1 \lambda_2} \mathcal{M}_{\vec{k}_1, \vec{k}_1 + \vec{q}}^{\lambda_3 \lambda_4} \right), \tag{13}$$

with the form factor:

$$M_{\vec{k}, \vec{k}_1}^{\lambda \lambda_1} = \left[\mathcal{U}_{\vec{k}}^\dagger \mathcal{U}_{\vec{k}_1} \right]_{\lambda \lambda_1} = \frac{1}{2} \left(1 + \lambda \lambda_1 e^{i(\theta_{\vec{k}} - \theta_{\vec{k}_1})} \right). \tag{14}$$

Here $\theta_{\vec{k}} = \text{atan}(k_x/k_y)$ is the angle of the momentum \vec{k} with respect to the x -axis. The Coulomb potential energy in the Fourier space reads as $V(\vec{q}) = 2\pi\alpha v_F/q$. Note that this collision integral can alternatively be determined by application of Fermi Golden's rule. The above Boltzmann equation was solved by the variational method [27] for shear viscosity of graphene at half-filling [4]. The same approach will be used here to calculate the current diffusion coefficient ζ . To this end, we first linearize the Boltzmann equation by the ansatz

$$f_\lambda = \tilde{f}_\lambda^0 + \delta f_\lambda. \tag{15}$$

In the presence of an external electric field, electrons and holes at CNP counter-propagate with opposite fluid velocity $\lambda \vec{u}$. Each of them forms individual fluids with the equilibrium distribution $\tilde{f}_\lambda^0 = \frac{1}{e^{(\epsilon_\lambda(\vec{k}) - \lambda \vec{u} \cdot \vec{k})/T} + 1}$. As a result, total charge current is given by

$$\vec{j} = Ne \sum_{\lambda=\pm} \int_{\vec{k}} \vec{v}_\lambda \tilde{f}_\lambda^0(\vec{k}) = en_{\text{th}} \vec{u} + \mathcal{O}(u^2), \tag{16}$$

with $N = 4$ accounting for valley and spin degrees-of-freedom and the number density of thermal excitations $n_{\text{th}} = \frac{4\pi T^2}{12v_F^2}$ remaining non-zero even at charge neutrality. In linear response, the deviation of the distribution function from the equilibrium δf_λ is linear in the shear force

$$X_{ij}^\lambda = \frac{\lambda}{2} \left(\partial_i u_j + \partial_j u_i - \delta_{ij} \vec{\nabla} \cdot \vec{u} \right). \tag{17}$$

This force is applied to the system via a current gradient $\partial_i j_j$ which amounts to the fluid velocity gradient $\lambda \partial_i u_j$. We write

$$\delta f_\lambda = \frac{g(\frac{\epsilon_\lambda(\vec{k})}{T})}{T} \frac{\lambda v_F k}{T} \left(\frac{k_i k_j}{k^2} - \delta_{ij} \right) f_\lambda^0(\vec{k}) \left(1 - f_\lambda^0(\vec{k}) \right) X_{ij}^\lambda, \tag{18}$$

with the dimensionless and unknown function $g(\frac{\epsilon_\lambda(\vec{k})}{T})$ to be determined by solving the linearized Boltzmann equation.

It is worth pointing out, as a comparison, that, in the calculation of shear viscosity [44, 45], electrons and holes form a single fluid and thus propagate with a joint fluid velocity \vec{u} . The equilibrium solution is instead given by $\tilde{f}_\lambda^0 = \left(e^{(\epsilon(\vec{k}) - \vec{u} \cdot \vec{k})/T} + 1 \right)^{-1}$ and the shear force in this case is given by $X_{ij} = \frac{1}{2} \left(\partial_i u_j + \partial_j u_i - \delta_{ij} \vec{\nabla} \cdot \vec{u} \right)$.

We determine the current diffusion coefficient ζ by computing the current flux:

$$\begin{aligned}
\mathcal{J}_{mn} &= Ne \sum_{\lambda} \int_{\vec{k}} \vec{v}_{\lambda m} \vec{v}_{\lambda n} \delta f_\lambda \\
&= Ne \sum_{\lambda} \int_{\vec{k}} \vec{v}_{\lambda m} \vec{v}_{\lambda n} \frac{g(\frac{\epsilon_\lambda(\vec{k})}{T})}{T} \frac{\lambda v_F k}{T} \left(\frac{\vec{k}_r \vec{k}_s}{k^2} - \delta_{rs} \right) X_{rs}^\lambda f_\lambda^0(\vec{k}) \left(1 - f_\lambda^0(\vec{k}) \right)
\end{aligned} \tag{19}$$

The current diffusion coefficient can be extracted from a constitutive relation:

$$\mathcal{J}_{xy} = \zeta \nabla_x j_y, \quad (20)$$

with

$$\zeta = \frac{1}{4n_{\text{th}}} \sum_{\lambda} \int_{\vec{k}} f_{\lambda}^0(\vec{k}) \left(1 - f_{\lambda}^0(\vec{k})\right) \frac{v_F^3 k}{T^2} g\left(\frac{\epsilon_{\lambda}(\vec{k})}{T}\right). \quad (21)$$

Solving the linearized Boltzmann equation for $g\left(\frac{\epsilon_{\lambda}(\vec{k})}{T}\right)$ by the variational method [4, 26, 27], we find the current diffusion coefficient of graphene resulting as

$$\frac{\zeta}{a^2 t} = C (\epsilon a t)^2 \frac{t}{T}, \quad (22)$$

with $C = 25.76$, and dimensions written explicitly using C-C hopping t as a unit of energy and graphene unit cell length a as a unit of distance.

II. COMPUTATION OF CONDUCTIVITY AND THE ROLE OF ADATOMS

II.1. Calculating the conductivity with QMC and the Stochastic analytical continuation method

Generally speaking, real-time dependent observables are difficult to measure with Quantum Monte Carlo (QMC) [36]. At equilibrium we have to rely on the analytical continuation [34–36] of the Euclidean current-current correlator, describing the reaction of the current density in a stripe defined by its coordinate x to the uniform electrical field in y direction applied to the whole sample:

$$G_{yy}(x, \tau) = \sum_{\substack{\langle i,j \rangle \in x \\ \langle m,n \rangle}} T_y^{ij} T_y^{mn} \text{Tr} \left(\hat{J}_{i,j} e^{-\tau \hat{H}} \hat{J}_{m,n} e^{-(\beta-\tau) \hat{H}} \right). \quad (23)$$

The current operator is defined as $\hat{J}_{i,j} = it \left(\hat{a}_{i,\sigma}^{\dagger} \hat{a}_{j,\sigma} - \hat{a}_{j,\sigma}^{\dagger} \hat{a}_{i,\sigma} \right)$. The normalization factor $T_y^{ij} = \vec{e}_{ij} \cdot \vec{e}_y$ takes into account the geometry of the lattice and direction of the bond \vec{e}_{ij} between sites i and j with respect to the electric field. The correlator (23) is computed using determinantal Quantum Monte Carlo [30–32]. We employ the ALF package [33], using the finite temperature QMC implementation with continuous fields with a Trotter decomposition step $\Delta\tau = 0.05$ in units of the inverse hopping t^{-1} . A typical sample has 12 lattice steps in the direction of periodical boundary conditions (see Fig. 1 in the main text) and varying width in the direction of open boundary conditions. Disorder is introduced along the open edges by randomly placing adatoms. We generate between 20 and 320 different configurations of adatoms (number depending on the lattice size) for each temperature and lattice, perform QMC simulations separately for each configuration of adatoms and subsequently average the results over them. The width of the samples is increasing with decreasing temperatures. A list of temperatures and corresponding lattice sizes can be found in Tab. I.

Stripes	18	21	24	27	30	34	36	45
βt	1.0	1.15	1.3	1.5	1.65	1.8	2.0	2.5
T/t	1.0	0.87	0.77	0.67	0.60	0.56	0.50	0.40
Samples	15	30	30	40	60	80	120	320

TABLE I. Simulated lattice sizes with corresponding temperatures and number of samples. In order to generate enough statistics to resolve the profiles in the lattice, we used a large number of samples for the larger lattices (lower temperatures).

The low frequency (hydrodynamic regime [26]) conductivity $\sigma(x, \omega = 0)$ can be subsequently extracted from the correlator (23) using the stochastic analytical continuation method (SAC) [34–36] exploiting the Green-Kubo relations:

$$G_{yy}(x, \tau) = \int_0^{\infty} K(\omega, \tau) \sigma(x, \omega) d\omega \quad (24)$$

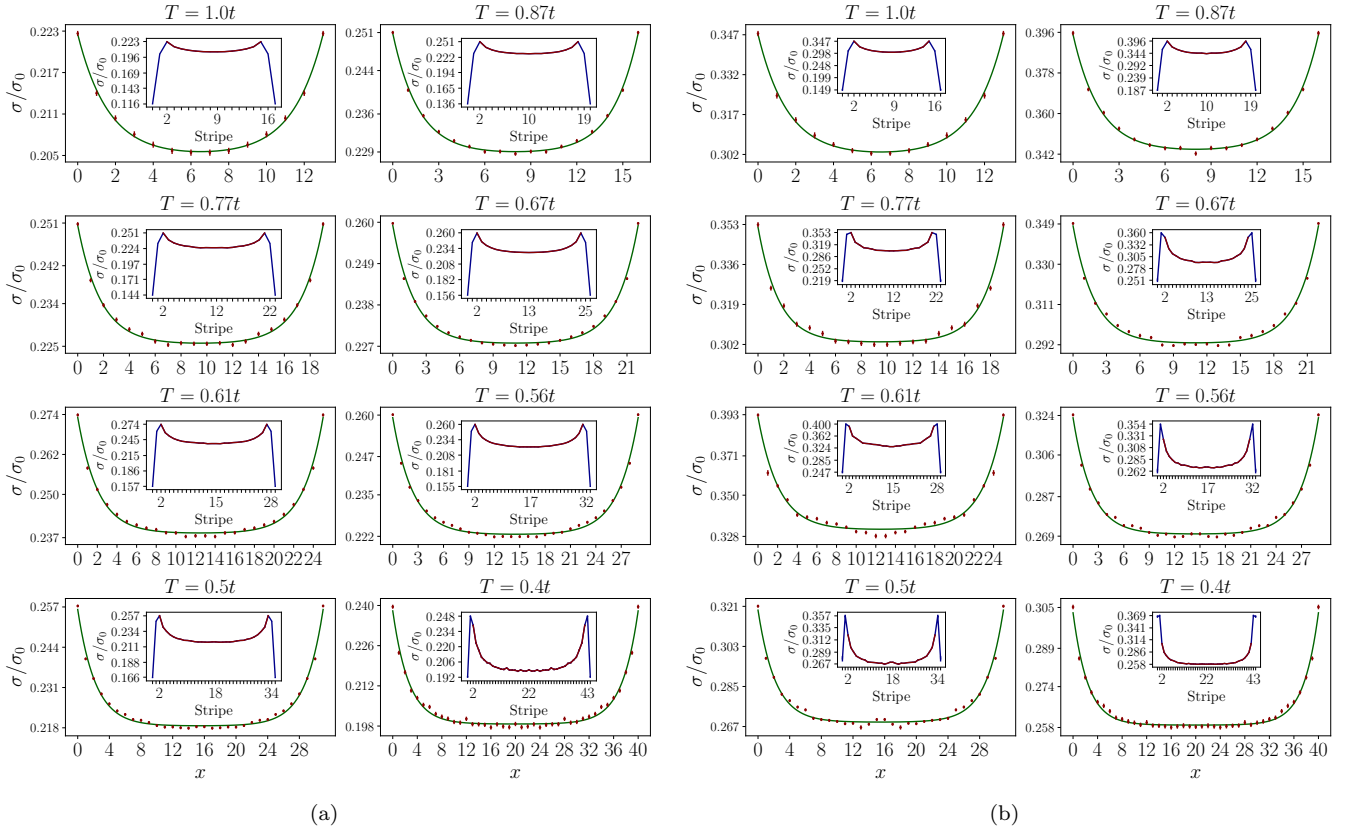


FIG. 4. Fitted conductivity profiles from the middle point of the correlator (a) and SAC (b) after averaging over all adatom configurations and symmetrizing around the middle of the sample. The raw data is shown as an inset for each profile, where the red curve corresponds to the data used for the fit (we start from the first point after the maximum). In the SAC case, the errorbars of each profile correspond to the error of the average over all adatom configurations. The fitting function (green) is the catenary curve from Eq. (6) in the main text.

with the thermal kernel $K(\omega, \tau) = \frac{2\omega \cosh(\omega(\tau - \frac{1}{2T}))}{\sinh(\frac{\omega}{2T})}$.

The resulting data for the DC conductivity, shown in Fig. 4(b) is then obtained by applying SAC to the QMC data of one given adatom configuration and consequently averaging over all configurations. The errorbars correspond to the error of the average over adatom configurations and the data is also symmetrized with respect to the middle stripe of the sample.

The low frequency conductivity can be also approximated by using the middle point of the current-current correlator (23) [40–42, 46]:

$$\sigma(x) \approx \frac{1}{\pi T^2} \int_0^\infty \frac{d\omega}{2\pi} \frac{2\omega\sigma(\omega)}{\sinh(\frac{\omega}{2T})} = \frac{1}{\pi T^2} G_{yy}(x, \beta/2) \quad (25)$$

These profiles are shown in Fig. 4(a). They are again obtained from averaging over the QMC data of all adatom configurations and symmetrizing around the middle-stripe.

Comparing the conductivity profiles calculated from the middle point of the correlator and SAC, we notice that they all agree well with the Eq. (6) in the main text. We observe finite size effects, such as small deviations from the smooth catenary curve (in particular for smaller temperatures), which also show up in small deviations from the power law in both SAC and correlator middle-point data (see Fig. 5). Nevertheless, as apparent from Fig. 5, the $1/T$ temperature dependence of the resulting current diffusion coefficient is evident in both cases. The similarities between the QMC and SAC profiles are also another marker for the smoothness of the frequency dependent conductivity $\sigma(\omega)$ at small ω , which is already visible in Fig. 6 (c). The remaining difference between correlator middle-point and SAC data (note the different values of the C coefficient in Fig. 5) can be attributed to the fact, that the resolution function $\frac{2\omega}{\sinh(\frac{\omega}{2T})}$ in (25) has in fact a finite width $\simeq T$, hence the approximate conductivity does not exactly correspond to the DC one.

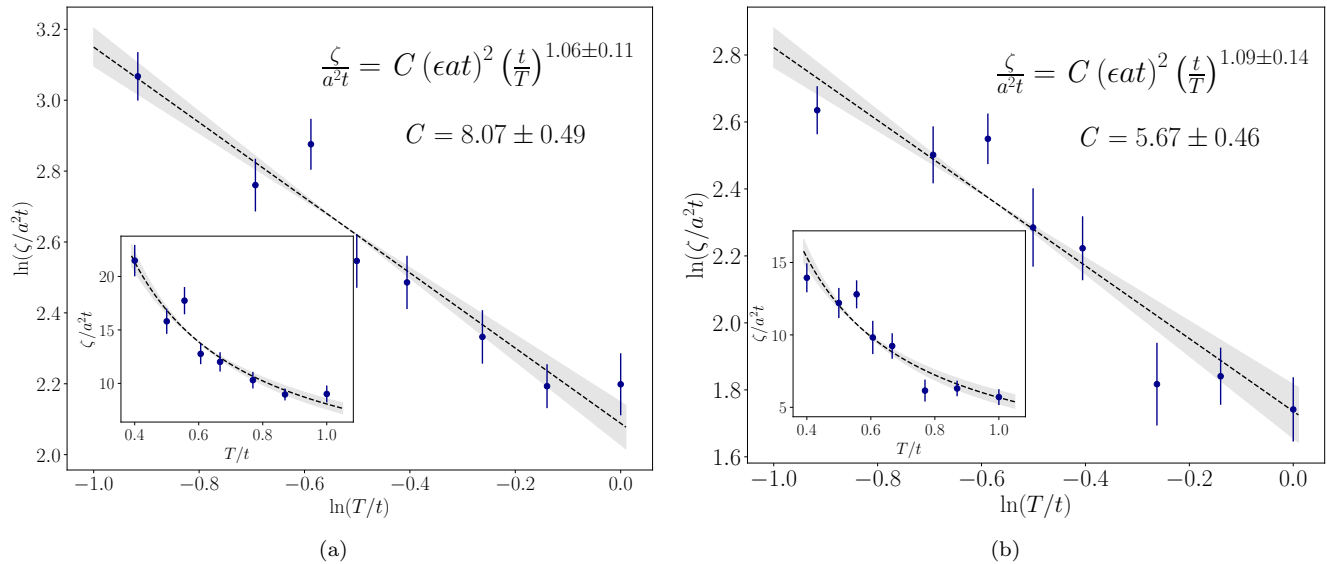


FIG. 5. Temperature dependent current diffusion coefficient ζ in log-log representation (main plots) and with linear scales (insets). The power law fit is shown with the dotted line. (a) Data is obtained from the conductivity profiles computed using the middle point of the current correlator (25). (b) Data is obtained using the full SAC spectral functions.

Despite these deficiencies, the usage of the middle point correlator can still be beneficial to recover the qualitative behavior of the low-frequency part of the spectral functions, because we can avoid larger fluctuations caused by the inherent instability of the analytical continuation techniques.

Summarizing, the qualitative behavior of the conductivity profiles across the sample and the temperature dependence of the current diffusion coefficient are independent on the underlying method for the conversion of the Euclidean current-current correlator into the low-frequency conductivity. It justifies the smoothness of the spectral functions at $\omega \rightarrow 0$ and supports the claim that our SAC results shown in the main text are valid despite the instability of the analytical continuation.

Next, we discuss in more detail the role of disorder imposed by adatoms on the formation of the boundary conditions.

II.2. Influence of adatoms on the conductivity

In order to quantify the effects caused by adatoms, we first look at the density of states (DoS) for a free tight-binding Hamiltonian (Fig. 6 (e)). Adatoms create localized near-zero and high-energy modes. The low-energy modes are located on the sites next to the ones where the adatom is attached, whereas the high-energy states belong to the adatoms themselves. These low-energy modes might be actually responsible for the inverse boundary conditions we already observed for the optical conductivity in the free case.

In order to understand this further, we computed the frequency-dependent free conductivity (see Fig. 6 (a) and (b)) for a lattice of 27 stripes (i.e. 648 orbitals) and the disorder configuration with 8 (2) adatoms on the edge (next-to-the-edge) stripes. Figure 6 (a) reveals a strong dependence of the profile on the frequency ω . The bulk conductivity is maximal at low frequencies $\omega \leq 0.2t$. This corresponds to the Drude peak (see (b)) which contributes significantly to the midpoint of the current correlator. The midpoint approximation (25) is therefore no longer valid and we expect inadequate results for an ideal non-interacting system. At larger frequencies around the Dirac-plateau regime $0.2t < \omega < 1.5t$, the profile is inverted, and the bulk conductivity reaches its minimal value whereas the edge conductivity is bigger. At $\omega \approx 1.8t$, the van Hove singularity results again in a higher conductivity in the bulk.

To verify that the midpoint of the current-current correlator is a valid estimator in the interacting case, we extract the conductivity using SAC from the QMC data of the above system size and compare it to the free case. The results in Fig. 6 (c) show that the Drude peak is indeed suppressed for the bulk conductivity, thus yielding a smaller value than at the edge for the whole frequency range. The boundary conditions have therefore the same effect on the conductivity profile as in the non-interacting regime with frequencies around the Dirac plateau, and the midpoint of the correlator is a valid estimator for the DC conductivity.

We should stress that our analysis is valid for suspended graphene. In typical hydrodynamic experiments however,

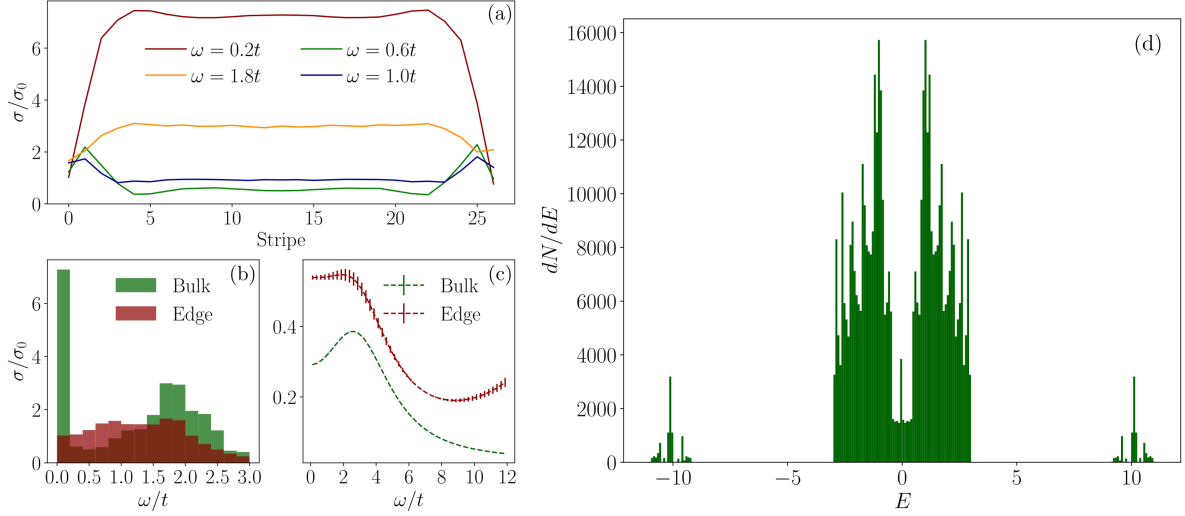


FIG. 6. Right: Density of states for the samples with width $L_2 = 90$ (45 stripes). We averaged the data over 20 samples with different configurations of adatoms at the edges to get a better energy resolution. Left: Frequency dependent free conductivity at the edge and bulk of a sample with 27 stripes (b) and its corresponding conductivity profiles (a). Bulk spectral function corresponds to the stripe coordinate 13 and edge spectral function corresponds to the stripe coordinate 0. (c) The frequency dependent conductivity of the same lattice but with interactions computed from SAC. Temperature is equal to $T = 0.77t$ for all calculations for this figure.

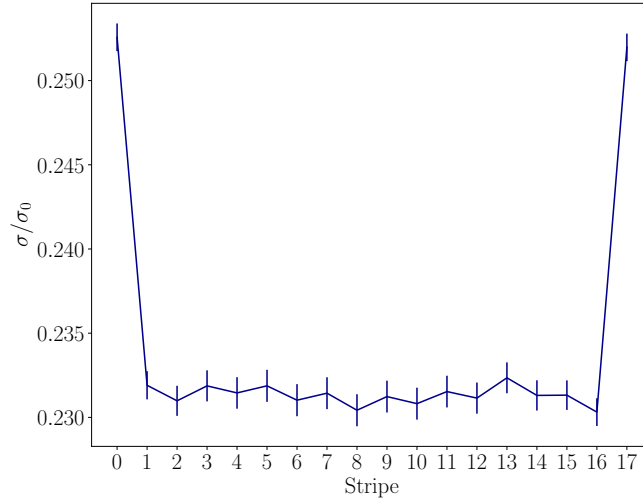


FIG. 7. Flat QMC conductivity profile of a lattice with open zigzag edges due to a low scattering rate between edge and bulk wavefunctions. Calculations are done at $T = t$ for the standard interaction strength corresponding to suspended graphene.

graphene samples are encapsulated between two layers of hexagonal boron nitride[12]. The Coulomb interaction is therefore weaker and the reduction of the Drude peak is less pronounced. As a consequence, the boundary conditions need to be reevaluated depending on the interaction strength. Also, with a weaker interaction, the approximation using the midpoint of the current-current correlator can become erroneous. However, we expect that the SAC processing remains stable at all interaction strengths.

Another important effect of the adatoms is that of a large scattering rate between the bulk and edge wavefunctions. Other types of boundaries, in particular zigzag boundaries have inherent zero modes as well, albeit without any disorder. In order for the boundaries to have an important effect on the conductivity profile, the scattering amplitude \mathcal{A} between the edge and bulk wavefunctions has to be sufficiently large. We call edge wavefunctions those which have the largest amplitude at the edge. They correspond to energies around $E = 0$ in the DoS on Fig. 6 (Right). Those

dominating within the bulk have larger energies $t > |E| > 0$. The scattering amplitude is proportional to the squared Coulomb interaction matrix element i.e. $\mathcal{A} \propto |\langle \Psi_{\text{Edge}} | V | \Psi_{\text{Bulk}} \rangle \langle \Psi_{\text{Edge}} | V | \Psi_{\text{Bulk}} \rangle|^2$, where V is the Coulomb interaction. We compare \mathcal{A} for a lattice with open zigzag boundaries and a lattice with disordered armchair boundaries used in the simulation on Fig. 4. In both cases we took a 18 stripes (=432 atoms) sample and averaged over all matrix elements between wavefunctions in the aforementioned energy intervals. In the disordered boundary case, we additionally averaged over samples with different configurations of adatoms. The scattering amplitude is on average 16 times larger for a system with disordered armchair edges. In order to further justify that the disorder generated by adatoms is responsible for the non-uniform conductivity profiles, we performed full QMC calculation also for the clean zigzag edge (Fig. 7). As one can see, the scattering amplitude between bulk and edge wavefunctions is indeed too small and we can only observe a flat conductivity profile in the bulk.

III. NUMERICAL EVALUATION OF \mathcal{E}_{\pm}^{mn}

For the computation of the current diffusion coefficient from the numerical data, it is necessary to calculate the diagonal element of $\mathcal{E}_{\pm}^{mn} = e \int d\vec{k} \partial_m v_{\pm}^n \tilde{f}_{\pm}$ (see main text) for the simulated lattices. In order to evaluate the integral over the discrete Brillouin-zone of our finite-sized lattices, we use the exact interacting Green Functions $G(\vec{k}, \nu_1, \nu_2, \sigma) = \langle \hat{c}_{\vec{k}\sigma\nu_1}^{\dagger} \hat{c}_{\vec{k}\sigma\nu_2} \rangle$ obtained in QMC for the evaluation of the distribution functions $\tilde{f}_{\pm}(\vec{k})$, where ν_1 and ν_2 correspond to the sublattice indices. More precisely we have

$$\tilde{f}_{\pm}(\vec{k}) = \langle \hat{\Psi}_{\pm}^{\dagger}(\vec{k}) \hat{\Psi}_{\pm}(\vec{k}) \rangle = \sum_{\sigma, \nu_1, \nu_2} \psi_{\pm, \nu_1, \sigma}^* \psi_{\pm, \nu_2, \sigma} \langle \hat{c}_{\vec{k}\sigma\nu_1}^{\dagger} \hat{c}_{\vec{k}\sigma\nu_2} \rangle \quad (26)$$

where $\psi_{\pm, \nu_1, \sigma}$ are the exact wavefunctions of holes (+) and electrons (-). obtained from the free tight-binding Hamiltonian.

For the evaluation of $\partial_m v_{\pm}^n = \partial_m \partial_n E_{\pm}(\vec{k})$ we use the free dispersion relation $E_{\pm}(\vec{k})$ of graphene, justified by only minor changes in the dispersion relations for the interacting case for the energies away of the Dirac point [47]. Therefore, the discretized integral for \mathcal{E}_{\pm}^{mn} becomes

$$\mathcal{E}_{\pm}^{mn} = \sum_{\vec{k} \in BZ} \partial_m \partial_n E_{\pm}(\vec{k}) \cdot \tilde{f}_{\pm}(\vec{k}) \cdot \Delta_{\vec{k}} \quad (27)$$

where the summation is carried out over the finite set of quantized \vec{k} points in the Brillouin-zone of the lattice and $\Delta_{\vec{k}} = |\vec{g}_1 \times \vec{g}_2|$ corresponds to the area element in the discretized \vec{k} -space. The unit vectors \vec{g}_1 and \vec{g}_2 are defined such that each discrete point \vec{k} in the Brillouin-zone can be accessed via $\vec{k} = n\vec{g}_1 + m\vec{g}_2$ with $n, m \in \mathbb{Z}$.

In Fig. 8 we compare the values of $\mathcal{E}_{\pm}^{nn} \equiv \mathcal{E}$ computed using the exact integral expression for the free case with the free tight-binding model computation on a finite sample, and with the full QMC calculation. We notice a quantitative difference of approximately 15% between the exact and tight-binding data even for the free system. This comes from the evaluation of \mathcal{E} on a finite-sized lattice. Thus the increase of lattice size for a given temperature should yield a better estimate. The inset (in Fig. 8) shows this, where the TB data points for \mathcal{E} at fixed temperature $T = t$ approach the exact integral with the increase of lattice size L . The obvious reason is that with the increase of the number of \vec{k} -points the evaluation of the integral via the sum becomes better and approaches the exact value for large lattice sizes. In general, we can conclude that the qualitative behavior of \mathcal{E} for our systems is in accordance with the exact result and only deviates by 15%. An additional observation is that at least for \mathcal{E} , our temperatures are still far from the Dirac point, where we expect \mathcal{E}/T to converge to $-2 \ln 2/\pi$. Finally, the figure also demonstrates that interaction effects become noticeable for \mathcal{E} only when approaching temperatures below $0.6t$. Despite being marginal, they have to be taken into account for a better estimation of ζ .

IV. CONTROLLING THE TRANSPORT REGIME

Within the framework of our microscopic description of graphene, we can distinguish between three types of electronic transport mechanisms, depending on the parameters of the microscopic Hamiltonian, temperature and lattice size.

Hydrodynamic regime, discussed extensively in this work, occurs when momentum conserving collisions between electrons dominate over all other scattering processes. In this regime, the conductivity profiles follow the continuum description from kinetic theory, despite being measured in QMC on a discrete grid, the lattice.

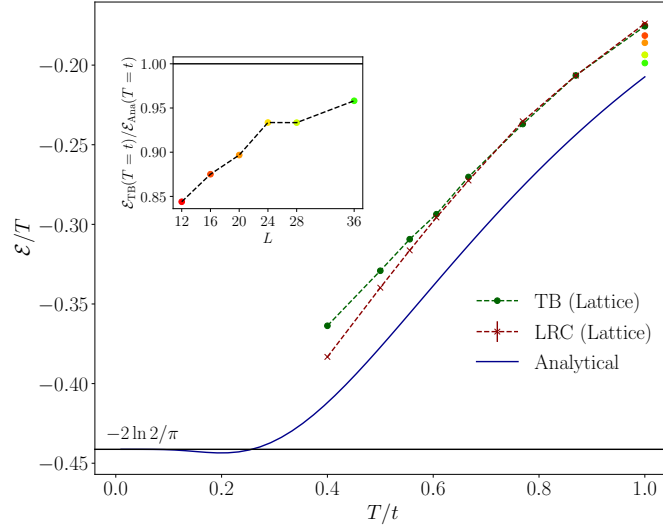


FIG. 8. Computation of \mathcal{E} . For the free case, we compare tight-binding calculation with the exact integral. Inset shows the convergence of the tight-binding \mathcal{E} towards the exact integral with increasing lattice sizes at $T = 1.0t$. Main plot shows both the free and the interacting (LRC) case.

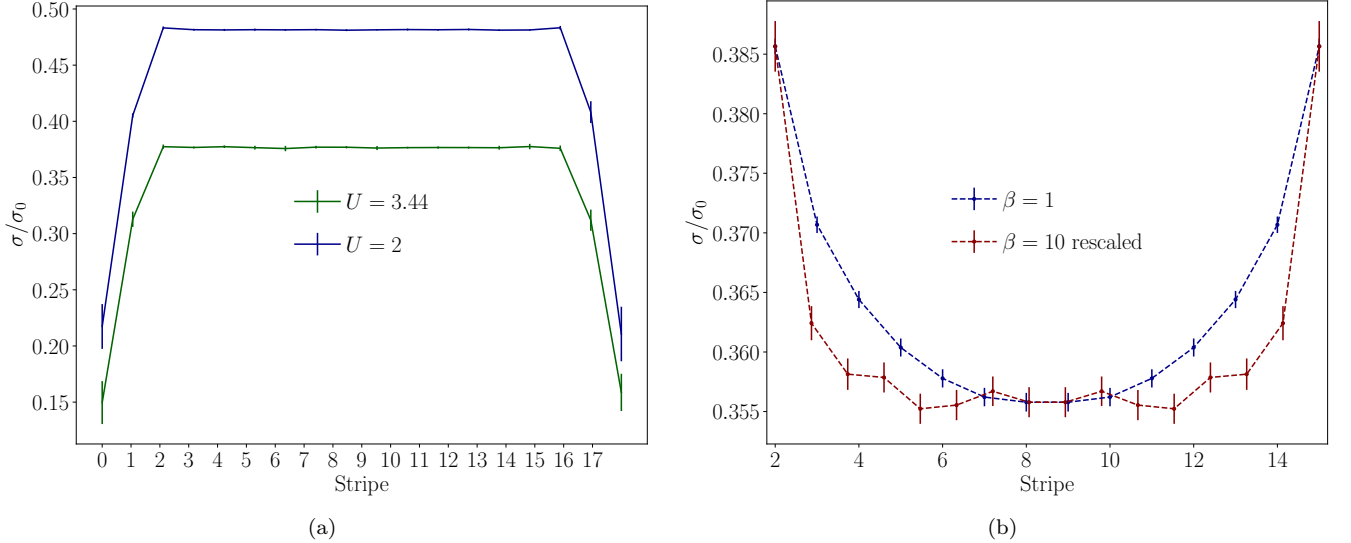


FIG. 9. (a) QMC conductivity profile for a system with only on-site Hubbard interactions $U = 2t$ and $U = 3.44t$. Temperature is equal to hopping and lattice geometry is the same as the $T = t$ LRC run. (b) Comparison between the QMC conductivity profiles for LRC runs on the lattice with 18 stripes at $T = 0.1t$ and $T = t$. The profile of $T = 0.1t$ has been rescaled to match the edge and bulk conductivity of the $T = t$ profile.

The hydrodynamic description is only valid if the electronic scattering length l_{ee} is significantly smaller than the width W of the samples. In the reverse case, we enter ballistic regime where the electrons effectively do not interact within the sample's volume and the continuum description becomes inadequate. This is equivalent to a decrease of the scattering amplitude which we can modify by keeping only on-site Hubbard interactions in our microscopic Hamiltonian.

Simulating this system, yields a flat conductivity profile, shown in Fig. 9(a), even for relatively large Hubbard interaction $U = 3.44t$, which is already quite close to the critical coupling of the Mott transition on a hexagonal lattice. Thus we can conclude that it is possible to switch from hydrodynamic to ballistic transport by turning off the Coulomb tail of the electron-electron interaction at fixed temperature and system size.

Choosing the correct temperature is also crucial for entering the hydrodynamic regime. The QMC scaling with system

size puts a strong limit on possible system sizes. Consequently, in order to have enough charge carrier excitations contributing to the transport and therefore conductivity, the temperature needs to be high enough (in other words, we should enter the regime $\omega < T$). Indeed, we can see in Fig. 9(b) that the QMC profiles, for a fixed lattice size but 10-times lower temperature, yields a flatter conductivity profile that does not follow the continuum description of kinetic theory. Thus the hydrodynamic transport can also be turned on and off by varying the temperature at a fixed interaction strength and system size, with lower temperatures leading to the suppression of hydrodynamic features of the electronic flow.

Finally, the third regime, diffusive transport, does not conserve momentum and is dominant when l_{ee} is larger than the diffusive scattering length scale l_{diff} (and $l_{diff} < W$). Even though the simulation of this situation is out of scope of this paper, we can still enter this regime by either enabling electron-phonon coupling to the microscopic Hamiltonian, or inserting adatoms over the whole lattice and not only the edges. With an increased density, we expect the conductivity to flatten until reaching an ohmic type of profile.

-
- [1] R. N. Gurzhi, *Soviet Physics Uspekhi* **11**, 255 (1968).
- [2] M. J. M. de Jong and L. W. Molenkamp, *Phys. Rev. B* **51**, 13389 (1995).
- [3] K. Damle and S. Sachdev, *Phys. Rev. B* **56**, 8714 (1997).
- [4] M. Müller, J. Schmalian, and L. Fritz, *Phys. Rev. Lett.* **103**, 025301 (2009).
- [5] A. Lucas and K. C. Fong, *Journal of Physics: Condensed Matter* **30**, 053001 (2018).
- [6] D. Y. H. Ho, I. Yudhistira, N. Chakraborty, and S. Adam, *Phys. Rev. B* **97**, 121404 (2018).
- [7] L. Levitov and G. Falkovich, *Nature Physics* **12**, 672 (2016).
- [8] F. Karsch, D. Kharzeev, and K. Tuchin, *Physics Letters B* **663**, 217 (2008).
- [9] P. K. Kovtun, D. T. Son, and A. O. Starinets, *Phys. Rev. Lett.* **94**, 111601 (2005).
- [10] D. A. Bandurin, A. V. Shytov, L. S. Levitov, R. K. Kumar, A. I. Berdyugin, M. Ben Shalom, I. V. Grigorieva, A. K. Geim, and G. Falkovich, *Nature Communications* **9**, 4533 (2018).
- [11] J. A. Sulpizio, L. Ella, A. Rozen, J. Birkbeck, D. J. Perello, D. Dutta, M. Ben-Shalom, T. Taniguchi, K. Watanabe, T. Holder, R. Queiroz, A. Principi, A. Stern, T. Scaffidi, A. K. Geim, and S. Ilani, *Nature* **576**, 75 (2019).
- [12] M. J. H. Ku, T. X. Zhou, Q. Li, Y. J. Shin, J. K. Shi, C. Burch, L. E. Anderson, A. T. Pierce, Y. Xie, A. Hamo, U. Vool, H. Zhang, F. Casola, T. Taniguchi, K. Watanabe, M. M. Fogler, P. Kim, A. Yacoby, and R. L. Walsworth, *Nature* **583**, 537 (2020).
- [13] A. Jenkins, S. Baumann, H. Zhou, S. A. Meynell, Y. Daipeng, K. Watanabe, T. Taniguchi, A. Lucas, A. F. Young, and A. C. Bleszynski Jayich, *Phys. Rev. Lett.* **129**, 087701 (2022).
- [14] E. I. Kiselev and J. Schmalian, *Phys. Rev. B* **99**, 035430 (2019).
- [15] K. Pongsangangan, T. Ludwig, H. T. C. Stoof, and L. Fritz, *Phys. Rev. B* **106**, 205126 (2022).
- [16] S. Sorella and E. Tosatti, *Europhysics Letters* **19**, 699 (1992).
- [17] M. Troyer and U.-J. Wiese, *Phys. Rev. Lett.* **94**, 170201 (2005).
- [18] M. V. Ulybyshev, P. V. Buividovich, M. I. Katsnelson, and M. I. Polikarpov, *Phys. Rev. Lett.* **111**, 056801 (2013).
- [19] M. Hohenadler, F. Parisen Toldin, I. F. Herbut, and F. F. Assaad, *Phys. Rev. B* **90**, 085146 (2014).
- [20] J. L. Jiménez, S. P. G. Crone, E. Fogh, M. E. Zayed, R. Lortz, E. Pomjakushina, K. Conder, A. M. Läuchli, L. Weber, S. Wessel, A. Honecker, B. Normand, C. Rüegg, P. Corboz, H. M. Rønnow, and F. Mila, *Nature* **592**, 370 (2021).
- [21] M. Ulybyshev, S. Zafeiropoulos, C. Winterowd, and F. Assaad, (2021), [arXiv:2104.09655 \[cond-mat.str-el\]](https://arxiv.org/abs/2104.09655).
- [22] P. Kovtun, *Journal of Physics A: Mathematical and Theoretical* **45**, 473001 (2012).
- [23] A. Lucas and K. C. Fong, *Journal of Physics: Condensed Matter* **30**, 053001 (2018).
- [24] B. N. Narozhny, *Annals of Physics* **411**, 167979 (2019).
- [25] L. Fritz and T. Scaffidi, *Annual Review of Condensed Matter Physics* **15**, 17 (2024).
- [26] L. Fritz, J. Schmalian, M. Müller, and S. Sachdev, *Phys. Rev. B* **78**, 085416 (2008).
- [27] J. Ziman, *Electrons and Phonons: The Theory of Transport Phenomena* (Oxford University Press, 2001).
- [28] M. Müller and H. C. Nguyen, *New Journal of Physics* **13**, 035009 (2011).
- [29] M. V. Ulybyshev and M. I. Katsnelson, *Phys. Rev. Lett.* **114**, 246801 (2015).
- [30] R. Blankenbecler, D. J. Scalapino, and R. L. Sugar, *Phys. Rev. D* **24**, 2278 (1981).
- [31] S. White, D. Scalapino, R. Sugar, E. Loh, J. Gubernatis, and R. Scalettar, *Phys. Rev. B* **40**, 506 (1989).
- [32] F. Assaad and H. Evertz, in *Computational Many-Particle Physics*, Lecture Notes in Physics, Vol. 739, edited by H. Fehske, R. Schneider, and A. Weiße (Springer, Berlin Heidelberg, 2008) pp. 277–356.
- [33] F. F. Assaad, M. Bercx, F. Goth, A. Götz, J. S. Hofmann, E. Huffman, Z. Liu, F. P. Toldin, J. S. E. Portela, and J. Schwab, *SciPost Phys. Codebases*, 1 (2022).
- [34] K. S. D. Beach, [arXiv e-prints](https://arxiv.org/abs/2004.04030), cond-mat/0403055 (2004), [arXiv:cond-mat/0403055 \[cond-mat.str-el\]](https://arxiv.org/abs/2004.04030).
- [35] A. Sandvik, *Phys. Rev. B* **57**, 10287 (1998).
- [36] H. Shao and A. W. Sandvik, *Physics Reports* **1003**, 1 (2023), progress on stochastic analytic continuation of quantum Monte Carlo data.
- [37] G. D. Mahan, *Many-Particle Physics*, 2nd ed. (Plenum

- Press, New York, 1990).
- [38] R. Kubo, *Journal of the Physical Society of Japan* **12**, 570 (1957), <https://doi.org/10.1143/JPSJ.12.570>.
 - [39] M. Jarrell and J. Gubernatis, *Physics Reports* **269**, 133 (1996).
 - [40] T. Stauber, P. Parida, M. Trushin, M. V. Ulybyshev, D. L. Boyda, and J. Schliemann, *Phys. Rev. Lett.* **118**, 266801 (2017).
 - [41] N. Trivedi, R. T. Scalettar, and M. Randeria, *Phys. Rev. B* **54**, R3756 (1996).
 - [42] D. L. Boyda, V. V. Braguta, M. I. Katsnelson, and M. V. Ulybyshev, *Phys. Rev. B* **94**, 085421 (2016).
 - [43] Jülich Supercomputing Centre, *Journal of large-scale research facilities* **5** (2019), 10.17815/jlsrf-5-171.
 - [44] M. Müller, J. Schmalian, and L. Fritz, *Phys. Rev. Lett.* **103**, 025301 (2009).
 - [45] K. Pongsangangan, P. Cosme, E. Di Salvo, and L. Fritz, *Phys. Rev. B* **110**, 045443 (2024).
 - [46] P. V. Buividovich and M. I. Polikarpov, *Phys. Rev. B* **86**, 245117 (2012).
 - [47] H.-K. Tang, I. Yudhistira, U. Chattopadhyay, M. Ulybyshev, P. Sengupta, F. F. Assaad, and S. Adam, *Phys. Rev. B* **110**, 155120 (2024).